SYNTHESIS AND CHARACTERIZATIONS OF EUROPIUM CHALCOGENIDE AND TELLURIUM NANOCRYSTALS

By

Weidong He

Thesis

Submitted to the Faculty of the

Graduate School of Vanderbilt University

in partial fulfillment of the requirements

for the degree of

MASTER OF SCIENCE

in

Interdisciplinary Materials Science

May, 2011

Nashville, Tennessee

Approved:

Professor James H. Dickerson

Professor Timothy P. Hanusa

ACKNOWLEDGEMENTS

I express my utmost gratitude towards Professor James H. Dickerson for providing me the opportunity to work on this project. I am grateful for his great guidance and patience in the research. I am also grateful to Professor Timothy P. Hanusa for his teaching and encouragement during this work. It was their guidance and encouragement that made this work possible.

I would like to thank Dr. Dmitry Koktysh and Dr. Suseela Somarajan for their help on the synthesis of EuS nanocrystals. I would like to thank Dr. Sameer Mahajan, Alex Krejci and Max Osmulski for their fruitful discussions and work in this project.

TABLE OF CONTENTS

LIST OF FIGURES

CHAPTER I

INTRODUCTION

There are two steps in crystal growth of NCs: nucleation and growth. In a colloidal synthesis, nucleation occurs at the initial stage of a reaction, where precursors are decomposed and very small objects start to form as nuclei for further growth. The size of nuclei is typically no larger than 2 nm. Once nuclei are present in a colloidal system, they will grow larger by diffusion of precursors and surface reaction on their surface. This step is called growth [1-2]. The synthesis of monodispersed NCs requires appropriate precursors, solvent, surfactants and reaction temperatures. By varying one or more of the factors, growth of NCs can have different mechanisms, typically varying between Oswald Ripening (OR) and Oriented Attachment (OA) Mechanisms [3].

Selection and Preparation of Precursors

In chemistry, a precursor is a material that reacts in a chemical reaction to produce a target material. For example, in a typical Au NP synthesis, tetrachloroauric acid is used as precursor to provide Au source. The selection of precursors is crucial to a NP synthesis since different precursors have different reactivities, giving rise to different activation energies for a synthesis [4]. If a precursor has a small decomposition activation energy,

nucleation will occur very rapidly, which suppresses the growth stage of nuclei, yielding small NCs. Otherwise, with a large decomposition activation energy, a precursor will tend to produce larger NCs. Therefore, the selection of appropriate precursor directly determines whether the synthesis of NCs will occur and whether the synthesis will yield a desired size distribution [5].

Before synthesizing a new NC, it is necessary to synthesize a precursor accordingly because such a precursor is often not available for the synthesis of a new nanomaterial. In this case, it is usually advised to design the new synthetic system based on the properties of the new precursor. Factors, such as appropriate solvents, surfactants and reaction temperatures, have to be chosen according to new precursors.

Surfactant as Stabilizer and Surface Ligand

In a colloidal synthesis, surfactants are compounds that are used to reduce surface tension between functioning agents in the system in order to facilitate the synthesis. When the synthesis ends, the surfactants can serve as surface ligands, which can form surface charges by ionization and dissolvation to prevent aggregation and protect the NCs if they are reactive in ambient conditions [6].

During the synthesis, the size of NCs is closely related to the amount of surfactants used. Addition of some surfactants can reduce the size of as-synthesized NCs while addition of others may increase their size. For example, in our previous research on the synthesis of EuS NPs, we found that the size of NPs increased with the amount of phenanthroline that was added. Phenanthroline was found to be able to facilitate the aggregation-mediated

growth of EuS NPs by its electronegative repulsion with negatively-charged oleate ligands on the surface of the NPs [7]. Figure 1 shows the TEM images of EuS NPs with

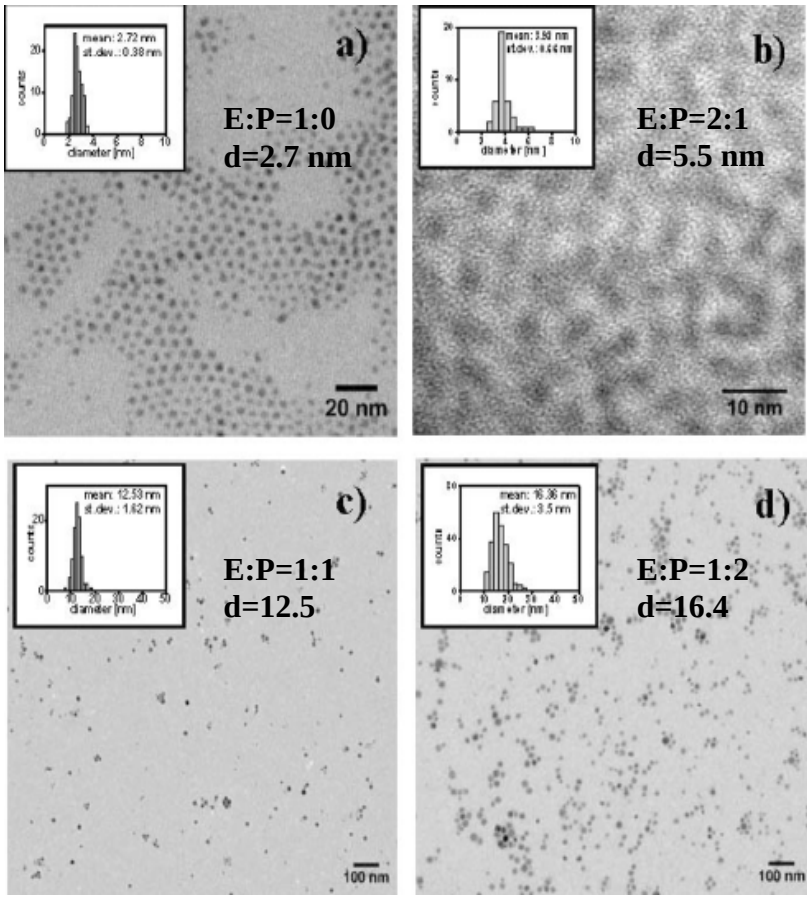

Figure 1 HR-TEM images of EuS nanocrystals grown at different synthetic conditions. Insets: EuS particle size histograms [15].

different size distributions achieved by changing the ratio of europium: phenanthroline (E:P) in the synthesis.

Oswald-ripening and Oriented-attachment Mechanisms

In colloidal chemistry, Oswald-ripening mechanism (OR) is an observed growth mechanism dominating lots of growth of colloids. In such a mechanism, small particles dissolve as a result of higher dissolvability and surface energy, and redeposit onto larger particles [3]. In an OR growth controlled by volume diffusion, the kinetics model is shown in Equation 1, where d_o is the diameter of precursor NPs, d_t the diameter of NPs at time t and k (m^3/min) reaction constant [8-10].

Oriented-attachment (OA) growth, directly from individual NPs, has been found to be an effective way to synthesize nanomaterials. In OA growth, NP monomers tend to attach to each other along a certain crystal orientation. Oriented attachment (OA) growth directly from individual NPs has been found to be an effective way to produce 1D nanomaterials [3]. OA mechanism is complicated considering its various kinetic models caused by the participation of multilevel particles in the reaction. Assuming reaction occurs between primary nanoparticle monomers, its kinetic model can be explained by Equation 1 [11].

$$d_t = \sqrt[3]{d_o^3 + kt} \qquad \text{Equation 1}$$

$$d_t = \frac{d_o\left(\sqrt[3]{2kt} + 1\right)}{kt + 1} \qquad \text{Equation 2}$$

Comparing Equation 1 and Equation 2, we easily find that d_t tends to reach a maximum in the OA model while it monotonously increases with time in the OR model. Therefore, combining time-evolved experimental data, the models can help to evaluate the growth mechanism of NR growth [11].

Europium Chalcogenide Nanocrystals

Both the spin configuration and the 4f-5d electronic transitions of europium (II) chalcogenides (EuX: X=O, S, Se, Te) make these materials promising candidates for advanced magnetic, optical, and electronic applications [12]. Among the europium chalcogenides, EuTe is a classical Heisenberg antiferromagnetic material, and EuS is a classical ferromagnetic material [12-13]. Interest in synthesizing nanoscale EuX has grown considerably during the past decade. Figure 2 shows the X-ray diffraction (XRD)

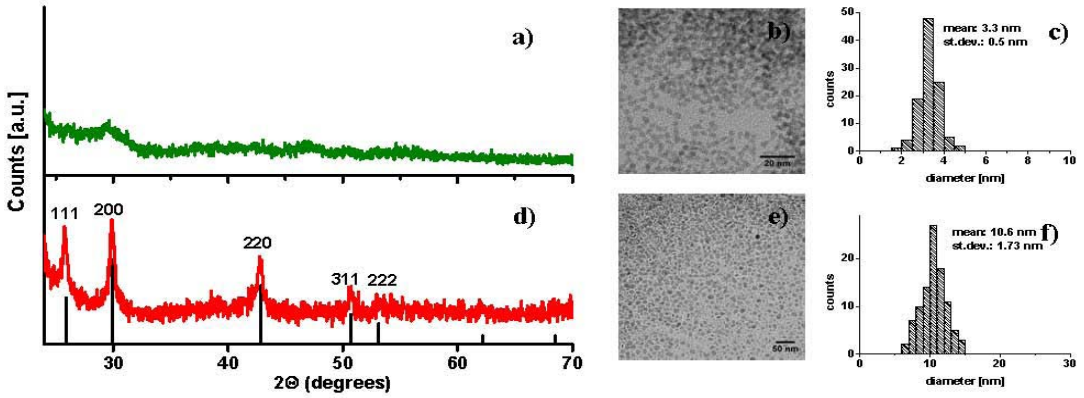

Figure 2 (a,d) XRD spectra, (b,e) TEM images and (c,f) size histograms of different size EuS NCs (a,b,c: 3.3 ± 0.5 nm and d,e,f: 10.6 ± 1.73 nm) [15].

patterns and Transmission Electron Microscopy (TEM) images of colloidal EuS NCs [13]. However, before our work, there had been no report on the synthesis of EuTe nanoparticles, which are as intriguing as the other EuX nanoparticles regarding their associated synthetic chemistry, optical and magnetic properties. Our research resolved this long-existing synthetic challenge by using facile chemistry method and, then by studying its nanoscale magnetic properties. Our efforts may open up the opportunity to explore EuTe on the nanoscale.

Recently more attractive is the synthesis of anisotropic EuX nanostructures such as EuO nanorods [14]. Dickerson's group at Vanderbilt University reported recently that the hot injection of EuS precursor could produce EuS nanorods [15]. However, it is difficult to identify the growth mechanism in the procedure due to the immediate nucleation and growth steps. Oriented attachment growth, directly from individual nanoparticles has been found to be an effective way to produce one dimensional (1D) nanomaterials [3].

To manipulate EuX nanomaterials with anisotropic structure, one must understand their formation mechanism [16]. Part of the research will synthesize anisotropic EuS and EuTe nanostructures using colloidal chemistry routes and, then, will focus on their formation mechanisms.

Tellurium nanocrystals

Burgeoning interest in novel green synthetic routes in nanocrystal colloidal chemistry have been motivated by employing the materials as building blocks for real-life applications [17-19]. One such material is tellurium (Te), given the abundance of

potential application for the material, such as gas sensors, thermoelectric and piezoelectric devices, photoconductors, optoelectronic devices, and organic synthesis [20-25].

Scope and organization of the thesis

For EuX (X=O, S, Se, Te), because the stable state of Eu in compounds is Eu^{3+}, it has been a challenge for researchers to synthesize these materials without oxidation before studying their properties and putting them into applications [26-30]. The as-synthesized NPs by a novel colloidal method in our research were then studied by X-ray diffraction, absorption spectroscopy and transmission electron microscopy, respectively. The results of these characterization measurements suggest that the synthetic method applied in the research could be adopted as one facile method to synthesize monodispersed EuS NPs. The feasibility of synthesizing monocrystalline EuS NRs by solvothermal synthesis was also demonstrated, making them potentially viable materials for device applications.

Colloidal EuO, EuS and EuSe nanoparticles (NPs) have been synthesized by a variety of groups [26-30]. However, there had been no report on the synthesis of EuTe nanoparticles, which are as intriguing as the other EuX NPs regarding synthetic chemistry, optical and magnetic properties. Dickerson's group in Vanderbilt University reported the first colloidal synthesis of EuTe nanostructures, using ethylene glycol (EG) as solvent and triethanolamine (TEA) as stabilizer, and the observation of nanocrystalline boundary effects on the magnetic response of these materials [31].

Among EuX, EuS and EuTe are classical ferromagnetic and antiferromagnetic materials with size-dependent optical properties, respectively. Therefore, the two materials can be served as platforms to facilitate the research on the magnetic and optical properties in general. Furthermore, the synthesis of reductive metal-nonmetal nanomaterials (EuS NCs) and that of metal-semimetal nanomaterials will shed new light on other EuX and metal based nanocompounds.

Contemporary work on nanoscale Te has yielded anisotropic structure, like Te nanotubes and nanowires [32-34]. However, substantial challenges remain to synthesize zero-dimensional Te nanostructures in a facile and environmentally friendly way, particularly considering tellurium's hexagonal crystallinity. Colloidal Te nanoparticles with two uniform size distributions have been synthesized in a one-step green chemistry method at room temperature. The surface ligands allow their isotropic growth, give rise to net surface charges in methanol suspension and make it feasible to fabricate Te NP films with good thickness and uniformity control.

Chapter II of the thesis focuses the syntheses of EuX and Te nanocrystals. Synthetic procedures will be presented. Chemical routes to EuS and EuTe nanocrystals with different size distributions are introduced. Chapter III covers a facile route to Te nanocrystals with binary size disturtions. In Chapter IV, taking EuS nanoparticles and nanorods as platforms, the growth mechanism of as-synthesized nanocrystals are analyzed. In Chapter V, the characterizations of as-synthesized EuX nanocrystals are discussed.

CHAPTER II

SYNTHESES OF EUX NANOCRYSTALS

Different groups have synthesized EuS using different methods [13]. In contrast to all previously reported solvothermolysis procedures involving the use of prepared single source precursor, a simple and cheap way to synthesize EuS NCs was proposed in the research. Through this method, monodispersed EuS NCs were successfully synthesized in one glovebox-free procedure without intermediate steps. EuS NPs of 2.5 nm to 19 nm were synthesized.

Colloidal Synthesis of EuS NPs and EuS NRs

Europium oleate was synthesized according to a previously reported procedure [35]. 2 mmol of Eu(III) chloride hexahydrate, 6 mmol of sodium oleate, 4 ml of ethanol, 3 ml of DI water, and 7 ml of hexane were mixed in a round bottom flask and heated at 60 °C for 4 hours. A top hexane layer containing europium oleate was isolated by separatory funnel and washed by DI water four times.

The synthetic steps for EuS fabrication were carried out in a Schlenk line. A mixture of 0.2 mmol europium oleate, 0.6 mmol of diethylammonium diethyldithiocarbamate, 0.2 mmol of phenanthroline, 1 ml of 1-dodecanethiol and 6 ml of oleylamine contained in a

25 ml three-neck flask was degassed, purged by argon at 80 °C, and subsequently heated to 320 °C under constant stirring. At this temperature, nucleation of EuS NCs was inititated as evidenced by the rapid color change of the solution from yellowish to purple. The solution was held at 320 °C for a period of time that depended on the desired size of NCs; thereafter, the solution was removed from the reaction vessel with a glass syringe. 10 ml of acetone was carefully added to a solution of EuS NCs. The resulting purple solution containing the EuS NCs was purified to remove unreacted precursors. The nanoparticles were first isolated by centrifugation and, after removing the supernatant, were redissolved in a small amount of chloroform. The above purification steps were repeated twice using acetone to precipitate the EuS NCs. Finally, the purified EuS NCs were dried under vacuum and redissolved in chloroform, yielding an optically clear purple solution. Anisotropic growth of the FCC EuS nanorods was achieved by using a 1:1 molar ratio of the same precursors used for EuS NCs and less dodecanethiol (0.1 ml). These parameters can significantly affect the surface energy of the different facets of growing EuS, leading to the formation of nanorods.

Colloidal Synthesis of EuTe NPs and EuTe NSs

All synthetic steps were carried out in nitrogen filled, moisture free glove box at room temperature. In the synthesis of 6.5 nm EuTe NPs, $EuCl_2$ (0.0446 g) was dissolved in a mixture solution of 15 mL ethylene glycol (EG) and 4 mL triethanolamine (TEA) under vigorous stirring. 2 mL of 0.1M solution of Na_2Te in EG were added dropwise into the vigorously stirred $EuCl_2$ solution. The resulting black-colored EuTe nanoparticles were

separated out via centrifugation, washed repeatedly with methanol, and finally stored in methanol for further measurements. The synthesis of 7.3 nm and 5.5 nm EuTe NPs is the same as that for 6.5 nm EuTe nanoparticles except that the concentrations of $EuCl_2$ and Na_2Te were 0.1 M and 0.4 M, respectively. In typical synthesis of EuTe NSs, 0.036 g phenanthroline was dissolved in 2 mL EG and injected into EuCl2/EG solution before the injection of Na_2Te/EG solution. Other parts of the synthetic procedure followed that of the 6.5 nm EuTe NPs synthesis.

The ease of TEA bonding to Eu^{2+} ions in the EG solution facilitated the formation of a chelate compound $[Eu(TEA)n]Cl_2$ in the early stages of the synthesis [36]. Upon injection of the EG solution of Na_2Te, EuTe NPs were formed, which readily precipitated in the reactor. Two reaction steps are associated with the formation of EuTe, as described in Scheme 1, which is consistent with the report from Xu et al on SnS [37]. The ligands

$$EuCl_2 + nTEA \xleftrightarrow{Stirring} [Eu(TEA)_n]Cl_2 \quad (1)$$

$$[Eu(TEA)_n]Cl_2 + Na_2Te \longrightarrow EuTe \downarrow + 2NaCl + nTEA \quad (2)$$

Scheme 1. Reaction schematic of EuTe colloidal synthesis

largely helped prevent EuTe oxidation in an oxygen present environment.

CHAPTER III

SYNTHESES OF TE NANOCRYSTALS

Tellurium nanoparticles were synthesized in a one-step fashion at room temperature by using sodium telluride (Na_2Te) as a precursor and oleic acid (OA) as an oxidizing agent in the presence of triethanolamine (TEA) dissolved in ethylene glycol (EG). Since all employed chemicals are environmentally friendly, this synthetic approach can be accomplished by green chemistry. Further, the synthesis yielded two distinct NP size distributions simultaneously.

Synthetic procedures

All synthetic steps were carried out in nitrogen filled, moisture free glove box at room temperature. In a typical synthesis, 3.5 mL oleic acid (OA) was dissolved in a mixture solution of 15.0 mL ethylene glycol (EG) and 4.0 mL triethanolamine (TEA) under vigorous stirring. 2.0 mL of 0.1 M solution of Na_2Te in EG was added drop-wise into the vigorously stirred OA solution. The resulting black-colored Te nanoparticles were separated by centrifugation, were washed with methanol, and were stored in methanol for further eletrophoretic depositions and measurements. This procedure produced the two size distributions described in the main text: 1.5 nm and 27.5 nm Te nanoparticles. To

achieve other binary size distributions, one can modify the concentration of Te precursor, decrease or increase synthetic temperatures, or terminate one synthesis at different times. In the synthesis, Na_2Te was oxidized by OA. Oxidized Te immediately nucleated into 1.5 nm Te NPs, some of which grew into sizes as large as 30 nm. Carboxylic acid oxidation balances the nucleation and growth steps, facilitating the formation of nuclei to promote surface reaction-limited kinetics at a low temperature once the nucleation of Te had completed. The Te nuclei grew into 27.5 nm NPs possibly through classical Ostwald ripening either by: a) the bulk phase diffusion of Te from the dissolution of 1.5 nm Te NPs due to their higher dissolvability compared to larger size NPs; or b) the rapid diffusion of multiple Te nuclei shortly after their formation. The latter mechanism is more plausible because of the mediated growth kinetics of our synthesis, which reached equilibrium for both NP sizes within a few hours. This mechanism is supported by theoretical calculations found in the recent literature that describes smaller NPs as leftover nuclei at equilibrium of the growth of larger NPs [38, 39]. Hexagonal Te NPs (space group $P3_121$, no. 152) were well liganded by TEA throughout the synthesis, passivating the primary [001] growth orientation observed in nanowires and, thus, facilitating the uniform growth of the material along all lattice orientations.

Structure characterizations of Te nanocrystals

Since the surface ligands contain –OH groups, Te NPs tended to aggregate so that NPs with the 2 diameters were not well separated after synthesis. We found that the number of times that methanolic suspensions of the NPs were cleaned, which comprised a

sonication step followed by a centrifugation step, determined how well we could separate the two NP size distributions. The cleaning process allowed us to precipitate the larger NPs while keeping the smaller ones in suspension. The cleaning procedure removes a portion of the surface ligands, asconfirmed by a decreasing FTIR signal for the C–C–O vibrations as well as C–O and C–N stretching as the number of cleaning times increased, weaken the van der Waals attraction between NPs, and eventually make smaller NPs dispersed in solvent. For example, 1.5 ± 0.5 nm NPs and 27.5 ± 5 nm NPs were optimally isolated by cleaning the samples three times, verified later by a Philips CM20 Transmission Electron Microscope (TEM) operated at 200 kV and X-ray diffraction (XRD). As seen in Figure 3c, 1.5 nm Te NPs were quasi-spherical with a slight elongation, which can be explained by the total number of hexagonal Te unit cells within a single 1.5 nm NP (approximately five).

As-dissolved Te from these small NPs diffused into other NPs through collision-based Ostwald ripening to grow into 27.5 nm Te NPs, the volume of which is approximately 8000 times that of 1.5 nm Te NPs. Despite aggregation, some individual 27.5 nm spherical Te NPs can be seen in the TEM image (Figure 3b). The increased aggregation as Te NPs grew implies that the liganding might be a dynamic process and interacted with NP growth until the growth of all lattice facets reached equilibrium.

XRD profiles of the colloidal Te NPs were taken to assess the crystallinity of Te NPs (Figure 3d). The XRD data of 27.5 nm Te NPs confirmed the presence of the primary Te crystal orientations. This demonstrates that the materials were well crystallized with hexagonal structure with space group of P3121. By evaluating the full width at half-maximum of the (101) peak and applying Scherer equation analysis, we determined the

diameter of the larger NPs to be 28.3 ± 2.3 nm. This size was consistent with that

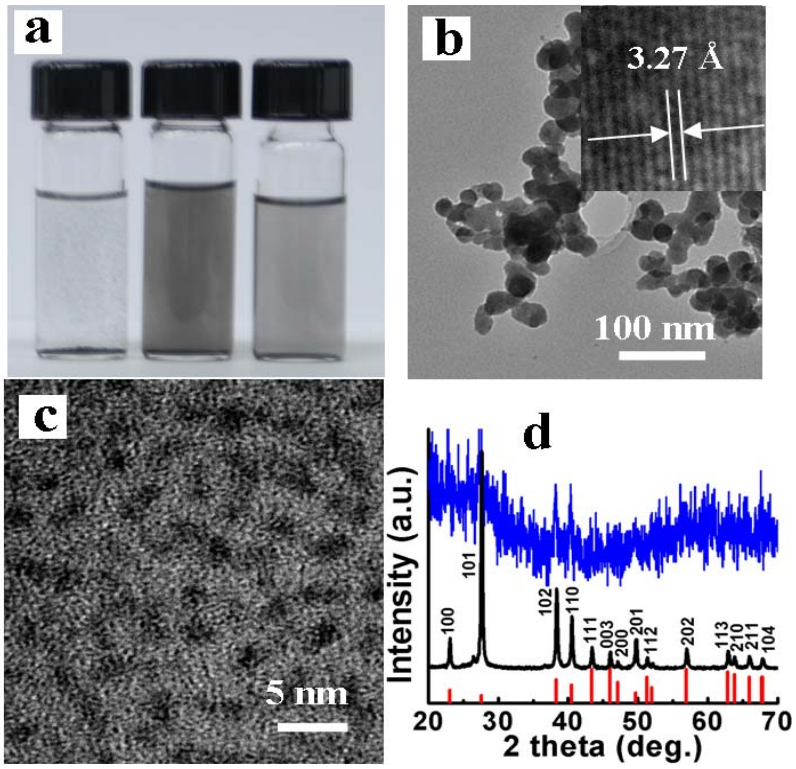

Figure 3 (a) Suspensions of Te NPs in methanol cleaned (left to right) once, twice, and thrice. (b) HTEM image of 27.5 nm Te NPs. Inset: HTEM image of (101) lattice spacings. (c) HTEM image of 1.5 nm Te NPs. (d) XRD spectra of 1.5 nm (top, blue) and 27.5 nm (middle, black) Te NPs. Primary peak locations for crystalline Te, provided by the JCPDS file (# 36-1452) of hexagonal tellurium, are indicated for clarity (bottom, red).

assessed from TEM images.

Electrophoretic deposition of Te nanocrystals

Electrophoretic deposition (EPD) was used to cast a film of Te NPs. We chose EPD because of its high rate of deposition, high controllability, scalability, uniform film casting capabilities, and the engendered low surface roughness of the films [40-42]. Others have shown the possibility of fabricating functional nanoparticle devices from the casts while maintaining the intrinsic quantum-confined characteristics of NPs [40]. The technique has been widely employed with colloidal NPs and has been demonstrated to be a way to test whether nanocrystals can serve as effective building blocks of device fabrication. For significant deposition to occur using our EPD approach, NPs should possess a net charge in suspension. EPD of Te films was conducted using 1cm x 2cm electrodes comprised of gold deposited on a Si substrate. Two electrodes were mounted in a parallel-plate configuration with ~4mm gap. With 10.0 V DC voltage applied, the electrodes were lowered about 1.0 cm into a 15.0 mL solution containing Te nanoparticle suspension in methanol. After ~20.0 min, the electrodes were raised from the solution and the voltage subsequently turned off after another 10.0 min. The cathode possessed a macroscopic film that was visible to the naked eye. The anode had no deposited film, indicating that only positively charged particles deposited onto the electrodes. We used methanol as the solvent in our experiments. The Te NPs rendered a positive charge as oxygen single bond of TEA was dissociated by methanol [43]. In the deposition, the net positive charge caused the Te NPs to move along the direction of applied electrical field. By changing the deposition time, films with different thicknesses, ranging from tens of nanometers up to several hundred nanometers, could be produced from the methanolic Te NPs suspensions. Atomic force microscopy (AFM; Figure 4a) and scanning electron microscopy (SEM; Figure 4b) images of films produced from 27.5 nm Te NPs highlight

an intriguing phenomenon that occurred during the deposition. Energy dispersive X-ray analysis (EDS; Inset of Figure 4b) were performed using Hitachi S-4200 Scanning Electron Microscope, which confirmed the presence of Te in as-deposited films. We observed that larger Te NPs, some upwards of 50 nm in diameter (Figure 4b), comprised a significant fraction of the EPD film. We attribute this apparent disparity in the nanoparticle diameter, seen in AFM and SEM *versus* that seen in TEM, to EPD-induced nanoparticle aggregation and growth. Such nanoparticle growth has been reported for other colloidal metallic nanoparticles (Au and Ag nanoparticle films), cast into films by electrophoretic deposition [44]. Unlike that reported for the EPD-facilitated growth of Au and Ag NPs, our Te NPs maintained their hexagonal shape during the EPD-induced crystal growth.

The thickness of as-synthesized Te NP film was 220 ± 29 nm, measured by a Veeco

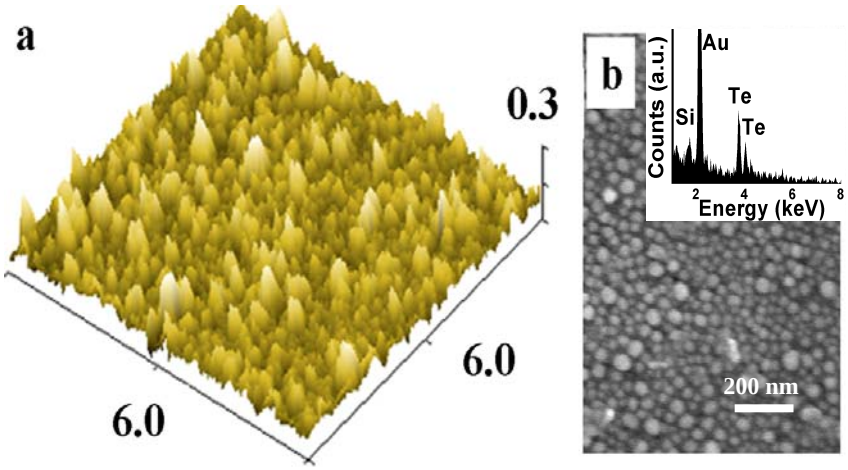

Figure 4 (a) AFM image of 27.5 nm Te NP EPD films deposited for 20 min. Scale unit: μm. (b) SEM image of as-deposited 27.5 nm Te NP film. EPD-induced growth of NPs, as large as 50 nm, can be seen.

Dektak 150 profilometer. The fabrication of Te NP films by EPD offers a route toward the facile implementation of colloidal tellurium nanostructures into device architectures.

CHAPTER IV

GROWTH MECHANISM OF EUS NANOCRYSTALS

2.5 nm EuS NPs were used as monomers to synthesize EuS NRs at different temperatures [45]. This chapter summarizes our analytical work on the growth mechanism of EuS NCs synthesized using EuS NPs as monomers based on the kinetic studies.

OA Growth Kinetics of Colloidal EuS NPs

We reported recently that hot injection of EuS precursor could produce EuS NRs. However, it is difficult to identify the growth mechanism in the procedure due to the immediate nucleation and growth. Oriented attachment (OA) growth directly from individual NPs has been found to be an effective way to produce nanomaterials. OA mechanism is complicated by its various kinetic models caused by the participation of multilevel particles in the reaction [11]. In order to study OA mechanism, a traditional mechanism, Ostwald ripening (OR), can not be ignored and the OA mechanism should be carefully distinguished from OR mechanism. In our research, a simple system was applied, that is, 2.5 nm EuS NPs with strong oleate surface ligands, and oleyamine as solvent. ransmission electron microscope (TEM, Philips CM20 at 200 kV) images 2.5 nm monodispersed EuS NPs were synthesized in a recently reported colloidal method

developed by the authors [15]. After synthesis, the NPs were cleaned with acetone for three times, and suspended in oleyamine/hexane mixture for following uses. The as-prepared suspension was then transferred into a glass reactor, and vacuumed under vigorous stirring at 80 ^{o}C for 45 min to remove hexane and other low boiling-point solvents. The vacuumed suspension was heated to target temperatures rapidly and under the protection of argon gas provided through Schlenk line. The reaction time was set at 3 hours for all experiments. Among the four temperatures, 300 ^{o}C, 310 ^{o}C, 320 ^{o}C and 340 ^{o}C, 300 ^{o}C was confirmed to be the nucleation temperature for EuS NP synthesis and 340 ^{o}C was the maximum temperature for oleyamine to stay stable. EuS NPs used in the research were covered by oleate ligand, which was confirmed by the result of Fourier transform infrared spectroscopy (FTIR) measurements on the NPs cleaned three times in Figure 5. In order to become dissolvable NPs, the ligand must be broken and detached

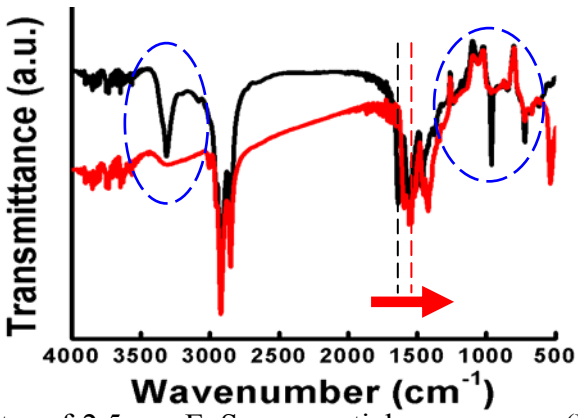

Figure 5 FTIR spectra of 2.5 nm EuS nanoparticle monomers (Black: oleate), and EuS nanocrystals synthesized at 320 ^{o}C (Red: oleyamine). Change from oleate to oleyamine is highlighted [45].

from the NPs [11]. The dissolubility of NPs in a solvent increases with the decrease in size at a certain temperature, so 2.5 nm EuS NPs should show a relatively high dissolubility in a solvent. However, if the NPs are tightly packed by oleate surface ligand, the actual dissolubility would be much lower than its theoretical value. Therefore, if the interaction between EuS NPs and long carbon chain oleyamine molecules is not that dominant, the NPs would stay undissolved and the mechanism would be an OA one. As shown in Figure 6-2b, dumbbell-shaped structures were formed at 300 ^{o}C although the size of EuS NPs in these structures remained 2.5 nm. By calculating the lattice spacing of the attachment planes as shown in the inset of Figure 6-2b, both lattice planes were assigned to be (200) which shows strong electron diffraction pattern as shown in the inset of Figure 6-2a. The unchanged size and oriented attachment of individual NPs indicate that the synthesis at 300 ^{o}C is confirmed to be an OA one [46, 47].

As temperature increased to 310 ^{o}C, chain-like structures were formed and these structures were arranged into 100-800 nm clusters, bigger ones of which are hollow inside, as shown in Figure 6-2c. Similar to that at 300 ^{o}C, the size of individual NPs stays at 2.5 nm, so the OA mechanism remains at 300 ^{o}C. However, at this temperature, EuS NPs interacted with each other more intensively compared with those at 300 ^{o}C so that more EuS NPs would be attached to each other to form chains. Since most ligands were still tightly bonded to the surface of NPs, charged NPs that were near repelled each other so that the NPs selectively attached each other at facets with relatively low ligand concentrations. Among the clusters, smaller ones tended to be solid maybe because some chains interacted with others in parallel by ligand attraction on their sides. When these solid clusters interacted with each other, they would again selectively attach to preferable

directions. Besides, at this temperature, oleyamine might be active enough to interact with oleate ligand on the NPs. Combining the two factors, the bigger clusters tended to be hollow to minimize their total surface free energy.

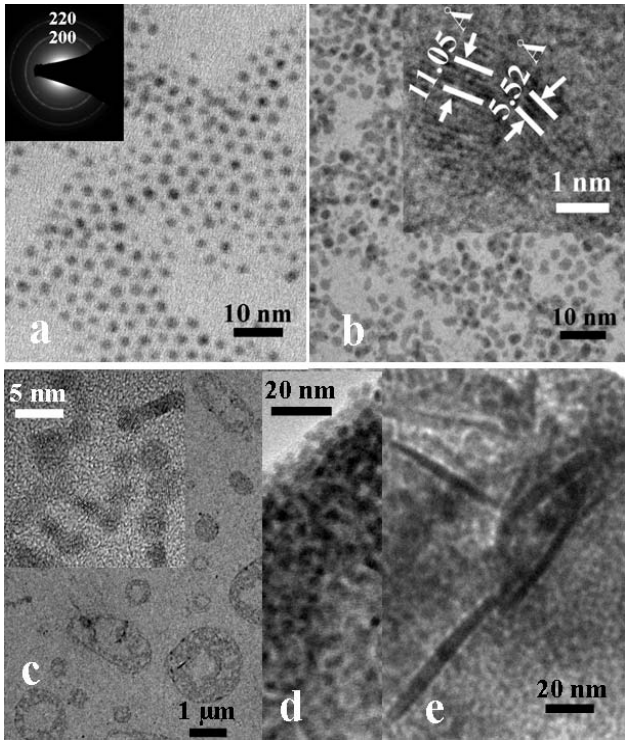

Figure 6 (a) TEM image and ED pattern of 2.5 nm EuS nanoparticle monomers, and TEM images of EuS nanocrystals synthesized at (b) 300 ^{o}C, (c) 310 ^{o}C, (d) 320 ^{o}C and (e) 340 ^{o}C [45].

As temperature was increased to 320 ^{o}C, which was the synthetic temperature of the NPs, the size of NPs increased from 2.5 nm to 3.1 nm and the NPs were attached in all directions and formed big aggregations, as shown in Figure 6-2d. Substituting d_t=3.1 nm, d_o=2.5 nm and t=180 min into both Eq.1 and Eq.2, their reaction constants are both

positive, which are 0.00084 min^{-1} and 0.079 min^{-1}, respectively. Letting t increase and using the same reaction constants, Eq.1 tends to reach a maximum at d_t = 6.7 nm while Eq. 2 gives a d_t value monotonously increasing with reaction time. OR is readily ruled out since monotonous increase in d_t was not observed in our experiments. This verifies that the synthesis at 320 ^oC applies an OA mechanism. OR might also occur due to the enhanced dissolvability and diffusivity of EuS in oleyamine, but would not be as dominant in a long time reaction [48]. Weakened ligand, higher dissolving and diffusing rate of EuS and increased thermal momentum of the NPs caused the ligand on EuS NPs to change from oleate to oleyamine, confirmed by the FTIR spectrum in Figure 6-1 (Red), as well as the aggregation to become dominant at this temperature.

Confirming the changes at 320 ^oC, some kinetic change above this temperature is expected. Figure 6-2e shows the TEM image of the sample at 340 ^oC, which shows that some NRs were among the NP aggregations. The diameters of NRs and NPs were both approximately 7.5 nm at t=180 min. Based on Equation 1 and Equation 2, OR mechanism is again ruled out in the long reaction time regime because the size of OR doesn't reach a maximum at experimental times. Substituting d_t=7.5 nm, d_o=2.5 nm and t=180 min, Eq.1 gives a k value of -0.0064 min^{-1}, which readily rules out the single-step monomer-monomer OA mechanism. Therefore, multilevel EuS NPs must participate in the OA reaction at 340 ^oC and the kinetic model is thus changed to give a faster growth rate [49, 50]. To calculate k at 340 ^oC, the experiment at 330 ^oC was done. At 330 ^oC, t = 180 min, d_t = 4.8 nm, and k is calculated to be 0.0056 min^{-1}. Combining the data from the experiment at 320 ^oC, k at 340 ^oC is calculated to be 0.035 min^{-1}. Allowing intermediate diameter and reaction time to vary with t = 180 min, d_t = 7.5 nm and k = 0.035 min^{-1}, a

two-step OA reaction mechanism works perfectly with the intermediate diameter and reaction time calculated to be 6.4 nm and 177 min, respectively.

Thermally-driven Formation of EuS NRs using EuS NPs as Monomers

As shown in Figure 6-2e NRs were also formed at 340 ^{o}C. Diffusion-dominated OA mechanism expects higher activation energy for high aspect-ratio NRs to form due to their decreased surface energy. For this sample with an aspect ratio of 15, the aspect ratio would be too high for the NRs to form if no other factors other than diffusion played a role in the synthesis. This brings out other factors, such as frequency factor A in the Arrhenius equation. It has been proved that this factor increases the aspect ratio of 1D nanostructures due to increased electric dipole-dipole interaction [51]. Both increased frequency factor and increased temperature made it possible for EuS NRs to be synthesized. Similar tapering extent for both ends of a NR, as shown in Figure 6-1e, indicates the OA reaction occurred at both directions along the NR with similar kinetics.

CHAPTER V

CHARACTERIZATIONS OF EUX NANOCRYSTALS

Bulk EuX compounds show temperature-dependent optical and magnetic properties. EuTe is a classical antiferromagnetic material with a Néel point around 9.6 K. EuO and EuS are FM, with Curie points at 66.8 K and 16.6 K, respectively. EuSe is metamagnetic with low-temperature ferromagnetic-AF transition. Optical and magnetic properties can be tuned by size due to quantum confinement. It is interesting to study how these properties of EuX vary with size on the nanoscale [13]. It is also interesting to study how dimensionality affects these properties. Some of this chapter focuses on the magnetic properties of EuTe NPs and NSs and the optical properties of both EuX NPs and 1 D EuX NCs.

Optical properties of EuX

EuX are optically interesting because their seven 4f electrons have different transitions upon excitation of incident light. Despite their different band gaps, all four EuX materials have two kinds of absorption peaks, as shown in Figure 7: a low-energy peak

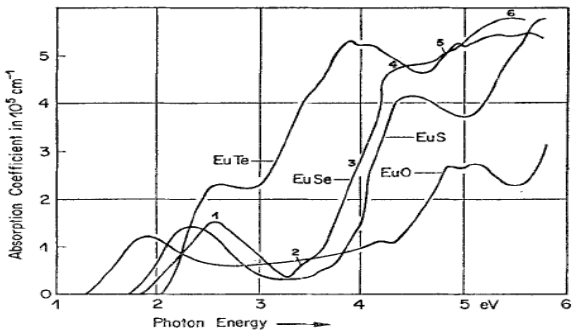

Figure 7 Absorption coefficient of the europium ehaleogenides at 300 K [13].

corresponding to $^4f_7(^8S_{7/2})$–$^4f_6(^7F_J)5d(t_{2g})$ transition of europium electrons, and a high-energy peak corresponding to from 4f levels to 5d states and the charge transfer between Eu(II) and Te(II) [13].

Superferromagnetism and Superantiferromagnetism

When the size of a magnetic material reduces to nanoscale, its magnetic properties might change dramatically. One interesting change is the change from multi-domain to single-domain based on Brown's theorem which states that magnetic domain formation is entirely suppressed in NPs because of the competition between magnetostatic energy and quantum mechanical exchange energy [52, 53]. Such a transition causes a material to

change from normal magnetic to super-magnetic. This subsection will focus on these super-magnetic terms originating from nanoscale magnetic materials.

Superparamagnetism is a phenomenon by which ferromagnetic and paramagnetic materials exhibit paramagnetic properties even below their Curie temperatures [54-58]. This phenomenon occurs only within a small length scale, typically when the materials are ~10 nm in size, with significant spins on their surface. When a material is superparagmagnetic, the energy barrier of aligning the magnetic moment of a particle is comparable to thermal energy. This makes the particles flip their magnetic moments much more randomly than would a bulk magnetic material. In this case, the interparticle magnetic interaction is weak, and the blocking temperature (below blocking temperatures, thermal energy becomes small and the magnetic moments become blocked) is related to $KV = 25\ k_B T_B$, where K is anisotropy constant, V is the volume of the particles, k_B is Boltzmann constant and T_B is blocking temperature. The energy barrier to align a particle along the direction of an applied magnetic field is expressed as $E_A = KV\sin^2\theta$, where θ is the angle between the easy axis (an energetically favorable direction of magnetization) and magnetization direction. As the size of a material reduces from bulk to nanoscale, the material changes from multi-domain to single-domain and then to sub single-domain. More energy is required to align the material as the material becomes single-domain, ending up with a higher coercivity due to a higher anisotropy constant. However, as the size is smaller than the critical single-domain size, due to the change in V, E_A will decrease, which will reduce the coercivity [13].

Similar to superparamagnetism, superantiferromagnetism occurs when the size of an antiferromagnetic material decreases below the single-domain size. Due to large

anisotropy energy (compared to Zeeman energy), the magnetization in superantiferromagnetism is significantly related to the uncompensated surface spins of the material, and for small applied magnetic fields it follows a non-Langevin dependence

$$m(H,T) = \chi_{\mathrm{AF}}(T)\ H + \frac{1}{\langle V \rangle}\int_{V_{\min}}^{V_{\max}} \times \mathrm{d}V f(V)\ \mu_{\mathrm{nc}}(V,T)\ G\left[\frac{\mu_{\mathrm{nc}} H}{k_{\mathrm{B}} T}\right] \qquad \text{Equation 3}$$

$$G(x) = \tfrac{1}{2}\int_0^{\pi} \mathrm{d}\theta \sin\theta \cos\theta \tanh(x\cos\theta) \qquad \text{Equation 4}$$

on the applied field as well as temperature, as shown in Equation 3. μ_{nc}(T, V) is the uncompensated moment of particle with volume V and f (V) is the volume distribution function of the particles, m (H, T) is magnetization, H is applied magnetic field, χ_{AF}(T) is antiferromagnetic susceptibility from cores of particles, k_B is Boltzmann constant, and T is temperature [59-62]. The second sum term on the right of Equation 3 represents the magnetization from uncompensated surface spins of the particles. The G function is expressed by Equation 4. There are two significant differences between superparamagnetism and superantiferromagnetism. First, superparamagnetism is characterized by the monotonous paramagnetic behavior of a material around the Curie point, for which the material in bulk form changes from paramagnetic to ferromagnetic as the temperature decreases. Superantiferromagntism is characterized by an extra increase

of magnetization as temperature decreases below the Néel point where the material in bulk form changes from paramagnetic to antiferromagnetic. In a normal antiferromagnetic material, such an increase of magnetization is absent as the material becomes antiferromagnetic from paramagnetic below Néel temperature. Second, similar to the difference between paramagnetism and antiferromagnetism, the magnetization in superparamagnetism is several orders of magnitude larger than that in superantiferromagnetism in which the susceptibility is on the order of 10^{-5} emu/Oe·g. The two differences between superparamagnetism and superantiferromagnetism, as stated above, are used to distinguish the two phenomena.

Characterizations of EuS NCs

XRD analysis verified the formation of EuS NCs. The diffraction peaks were indexed and juxtaposed with the JCPDS file for bulk EuS (JCPDS, pdf file 26-1419). EuS possesses a rock salt crystallinity with a lattice constant of 0.5968 nm (Figure 8). As confirmed by the XRD analysis, an increase in the diameter of the NC yielded ever increasingly sharp XRD peaks. Broadening is related to the formation of small size NCs compared to bulk material. No additional peaks due to impurities or surface oxidation were observed.

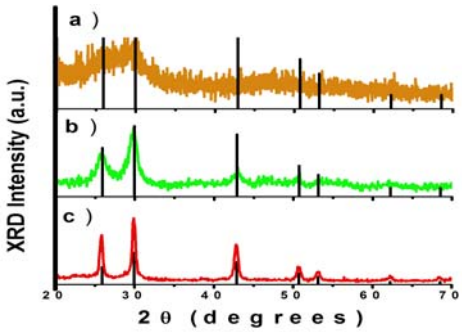

Figure 8 Powder X-ray diffraction patterns of (a) 5 nm, (b) 10 nm, and (c) 25 nm EuS nanocrystals. Bragg diffraction peaks from bulk EuS (JCPDS 26-1419) are presented for comparison [15].

he characterization of the EuS NCs using HRTEM, as shown in Figures 9a-d, revealed a predominance of monodisperse spherically-shaped nanoparticles with sizes below 20 nm. The particle's sizes can be controlled in a wide range with the smallest one down to 2.5 nm. The calculated average diameter of the nanocrystals, determined from representative TEM micrographs, were 2.5, 5, 12, 19. The use of different growth times and different concentrations of phenanthroline and dodecanethiol allowed precise control of the mean diameter. Increasing the reaction time prior to quenching, decreasing the concentration of dodecanethiol, and increasing of the concentration of phenanthroline facilitated the growth of larger NCs. Dodecanethiol served as the primary growth control and ligand agent and provided the most reliable results in terms of sample monodispersity and particle size control. The size tuning of EuS NCs can be explained by the high degree of control over nucleation and growth stages and low degree of Ostwald ripening that our synthesis procedure provided.

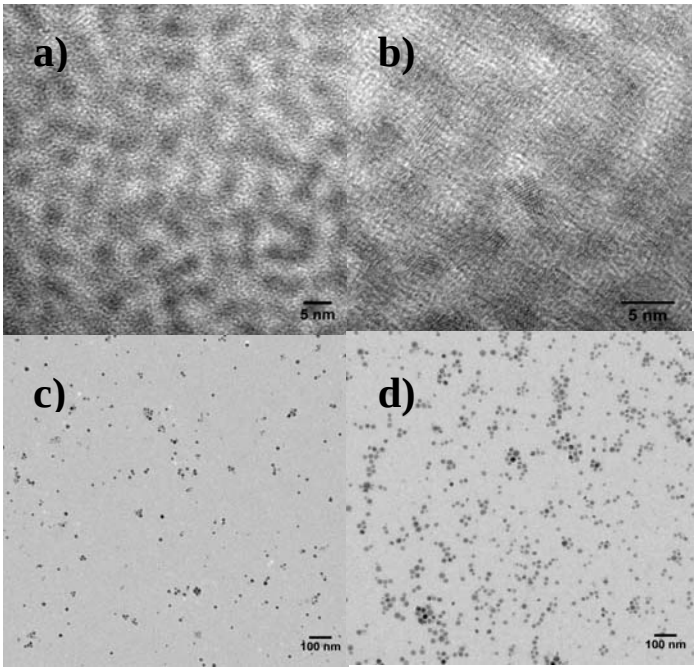

Figure 9 HRTEM images of EuS nanocrystals grown at different synthetic conditions: (a) 2.5 nm, (b) 5 nm, (c) 12 nm and (d) 19 nm [15].

Room temperature optical absorption spectra of EuS NCs solutions, suspended in chloroform, are shown in Figure 10. There are two major peaks corresponding to different types of electronic transitions. The low energy absorption peak corresponds to the $4f^7$-$4f^6 5d^1$ transition, whereas the high-energy absorption peak (Figure 5-4. Inset) corresponds to the $4f^7$-$4f^6$ transition and charge transfer between Eu(II) and S(II) [4, 16, 8]. As different particles sizes were synthesized, the absorption peaks positions blueshifted towards higher energies with decreasing particle's size [13]. We observed a shift from 510 nm for 25 nm EuS NCs to 490 nm for 2.5 nm EuS NCs which can be explained by quantum confinement [13].

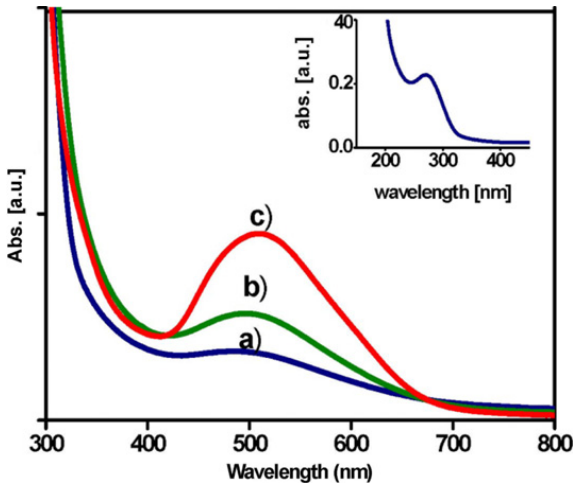

Figure 10 Optical absorption spectra of (a) 2.5 nm, (b) 5 nm, (c)12 nm EuS nanocrystals in chloroform. Inset: high-energy absorption peak of 2.5 nm EuS NCs [15].

Characterizations of EuTe NCs

Typical transmission electron microscope (TEM) images of EuTe NPs are taken (Figure 11a). As seen from the images, the NPs were nearly spherical. Clear lattice fringes corresponding to the (200) plane of EuTe, confirmed the crystallinity of the sample (Figure 11b). The NP size distribution is given in the histogram; the average size of the NPs, 6.5 nm ± 1.7, corresponded to $EuCl_2$ and Na_2Te concentrations of 0.20 M (Figure 11c). Similarly, we synthesized NP samples from 0.10 M and 0.40 M concentrations that yielded average diameters of 7.3 nm ± 1.7 nm and 5.5 nm ± 1.5 nm, respectively, evidenced by the size distribution histograms of the two samples. The fact that high concentrations of starting materials tend to yield smaller EuTe NPs is consistent with Reiss's prediction on the size-distribution of particles [63]. The electron diffraction in Figure 11d showed well-resolved lattice planes that correspond to the (111), (200), (220), and (222) planes of cubic EuTe, which is in good agreement with the XRD data.

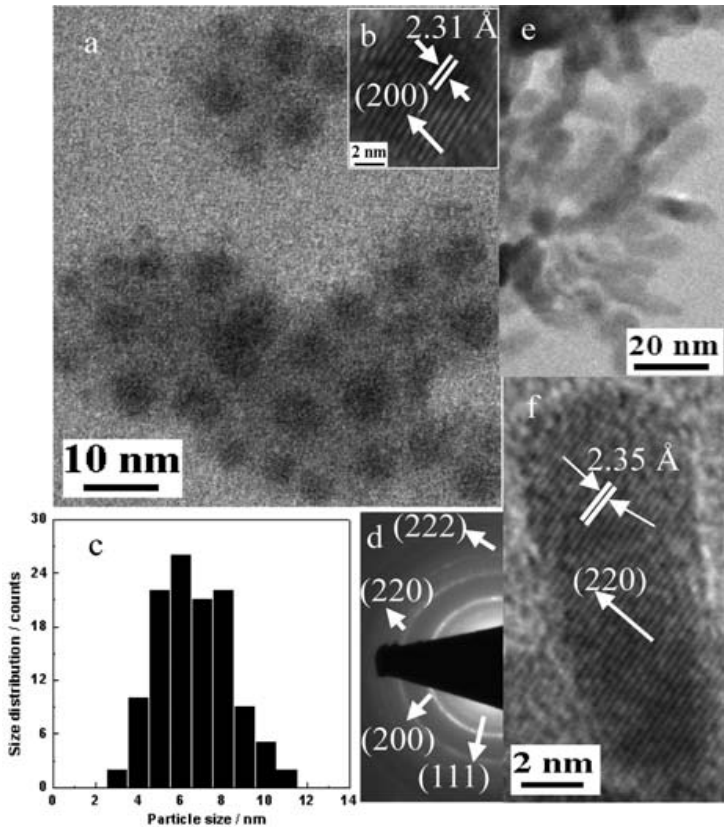

Figure 11 (a and b) TEM images of 6.5 nm crystalline EuTe NPs. Average diameter is 6.5 nm. Circles are to guide the eye. (c) Histogram of NP size distribution. (d) Electron diffraction pattern of FCC EuTe NPs. (e and f) TEM images of EuTe NSs [31].

From the TEM images of as-synthesized EuTe NSs, the NSs are 6.8 nm in diameter and 20.4 nm in length (Figure 11e-1f). The observed lattice spacing was 2.34 Å, which corresponds to the (220) plane (Figure 11f). The formation of as-synthesized anisotropic EuTe NSs was driven by surface packing of phenanthroline. Before or during nucleation, electron-rich phenanthroline self-organized into elongated reverse micelle-like structure, similar to what were proposed on the formation of Au and CdSe NRs [64]. The elongated

nuclei resulted in different packing densities of phenanthroline on different lattice planes of EuTe crystals, which resulted in the different growth rates along different crystal orientations and facilitated the anisotropic growth.

X-ray diffraction spectra of the colloidal EuTe NPs and NSs provide complementary affirmation of the formation of highly crystalline EuTe nanocrystals (Figure 12a). All our samples have the dominant peak at 2θ = 27.7º, which is assigned to (200) lattice of

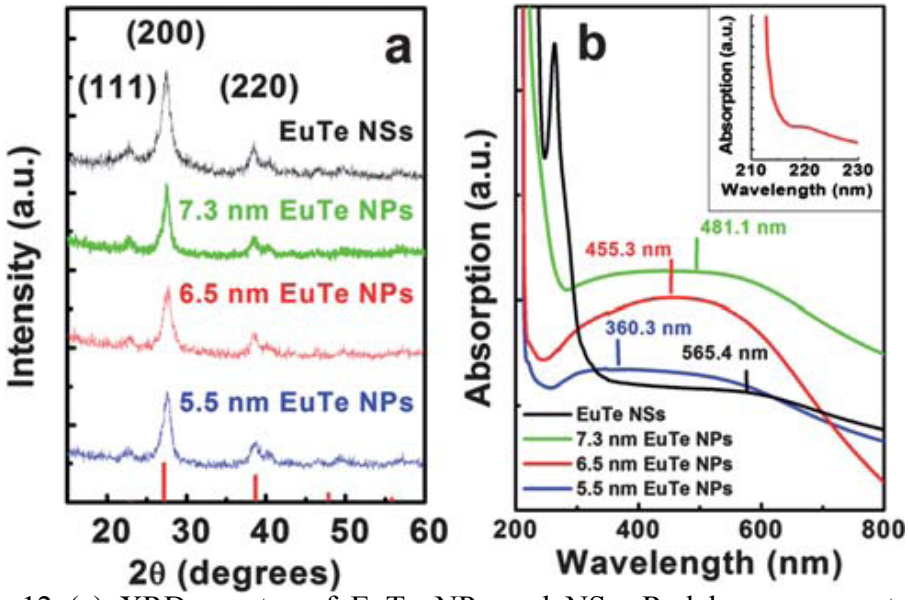

Figure 12 (a) XRD spectra of EuTe NPs and NSs. Red bars represent primary diffraction peaks of EuTe from its JCPDF file. (b) Absorption spectra of EuTe NPs and NSs in methanol. Inset: absorption of 6.5 nm NPs exhibiting transitions from 4f levels to 5d states and the charge transfer between Eu(II) and Te(II) [31].

NaCl-type EuTe. Two smaller peaks are also observed at 2θ=40.0º and 2θ=49.6º; we attributed those peaks to metallic tellurium that formed on the surface of the EuTe nanocrystals through the oxidation of EuTe when exposed to air. By evaluating the full

width at half-maximum of the (200) peak and applying the Scherer equation, the diameters of the 7.3 nm, 6.5 nm and 5.5 nm NPs (determined by TEM) were calculated to be 9.5 nm, 7.2 nm and 6.5 nm, respectively. The 20 nm long EuTe NSs was calculated to be 16.3 nm. These sizes are consistent with those calculated from TEM images.

There were two peaks for both EuTe NPs and NSs; the low-energy peak corresponded to $4f^7$–$4f^6$ (^7F_J) 5d (t_{2g}) transition of europium electrons and the high-energy one around 200-300 nm, corresponded to the transitions from 4f levels to 5d states and the charge transfer between Eu(II) and Te(II) (Figure 12b (Inset)). A blue shift of the absorption peaks was observed as the NP size decreased from 7.3 nm to 5.5 nm, which was attributed to quantum confinement effects. Interestingly, the high energy absorption peak of EuTe NSs appeared to be much stronger than the corresponding peak for EuTe NPs. This was likely due to a relative blueshift of the high-energy 4f-electron in the zero-dimensional, quantum-confined NPs (at ~220 nm) versus in the one dimensional NSs (at ~250 nm). The increased length of the EuTe NSs (~20.4 nm) inhibits quantum confinement affects along their major axis, hence, redshifting their absorption peak relative to the NPs.

The magnetic properties of as-synthesized EuTe NPs were studied by vibrating sample magnetometry with a Quantum Design Physical Property Measurement System. Zero-field-cooled and field-cooled magnetization measurements on 6.5 nm EuTe NPs from 50 K to 2 K were conducted (Figure 13). Although bulk EuTe is antiferromagnetic with a Néel temperature of 9.6 K, both ZFC and FC measurements from 2 K to 50 K did not exhibit such a paramagnetic to antiferromagnetic transition for 6.5 nm EuTe nanocrystals. To study the magnetic response of the EuTe sample directly, field-cooled magnetic

susceptibility was plotted versus temperature and compared to the Curie-Weiss law (Figure 13, (Inset)). Between 10 K and 20 K, the slope of a linear fit to the χ^{-1} versus temperature graph changes markedly (denoted by the dotted horizontal line). As the

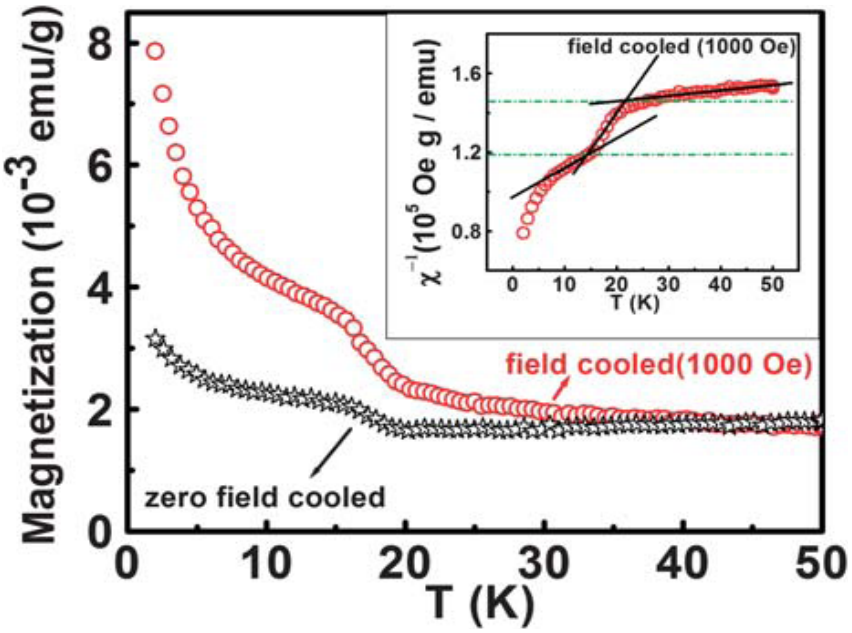

Figure 13 ZFC and FC (at 0.1 T) curves of 6.5 EuTe NPs from 50 K to 2 K. Inset: field-cooled inverse magnetic susceptibility versus temperature of 6.5 nm. EuTe NPs [31].

temperature increases to 15 K, the x-axis (temperature) intercept of the linear fit changes from a large negative value to positive value. The intercept shifts back to a large negative value around 20 K. This evolution is atypical for normal antiferromagnetic or superparamagnetic nanomaterials. This phenomenon could be reconciled as being influenced by the presence of uncompensated spins on the surface of these nanometer-

sized EuTe particles, thus making them prime candidates for being superantiferromagnetic [65]. Under finite-size effects, the two observed transitions might be shifts between superantiferromagnetism and superparamagnetism, given the small mass susceptibility in range. Systematic magnetic study of EuTe NPs and NSs is the subject of future research.

CHAPTER VI

CONCLUSION

We developed a technique where EuS NCs were synthesized by a direct solvent thermolysis of europium oleate and diethyldithiocarbamate in oleylamine in the presence of dodecanethiol and phenanthroline. Monodispersity, size and shape control were achieved by tuning the synthetic conditions. The optical properties of fabricated EuS NCs were found to be size dependent.

Colloidal EuTe NPs and NSs have been synthesized for the first time, and the magnetic properties of EuTe NPs have been introduced. This facile room temperature colloidal synthesis helps to overcome the challenges of synthesizing other rare-earth chalcogenides and facilitates the studies on these materials in nanoscale. The observation of superantiferromagnetism in the nanomaterials presents a rare opportunity to investigate unique size-dependent magnetic phenomena. Our synthetic technique also provides the potential of implementing EuTe NPs and NSs in a host of magnetic, photovoltaic, and magneto-optical device applications.

Our work reports a colloidal synthetic method of nanocrystals with binary uniform size distributions in one synthesis. This binary synthetic method of inorganic nanocrystals was accomplished for the first time, and thus has fundamental significance to compound synthesis community. Tellurium nanocrystals synthesized with this method were shown

to have good application potentials indicated by the ease of making them into macro-sized films by eletrophoretic deposition technique. Therefore, this method facilitates the efficiency of making applicable nanomaterials and opens the opportunity to design synthetic methods giving multiple size distributions.

Clusters of EuS nanocrystals were synthesized through an oriented attachment mechanism by thermally annealing 2.5 nm EuS NCs liganded with oleate. An increase in thermal energy changed both the ligand and reaction constant, which gave rise to a multilevel OA mechanism that produced high aspect-ratio EuS nanorods. These results will help to improve our understanding of both OA and OR growth mechanisms, and may assist in the synthesis of nanoclusters and NRs of other nanomaterials.

REFERENCES

1. Z.A. Peng, X.G. Peng, *J. Am. Chem. Soc.* **2002**, 124, 3343.

2. Zeng, J., Huang, J., Liu, C., Wu, C. H., Lin, Y., Wang, X., Zhang, S., Hou, J. and Xia, Y. *Advanced Materials* **2010**, 22, 1936–1940.

3. Zhang, J.; Huang, F.; Lin, Z. *Nanoscale* **2010**, 2, 18–34.

4. Wagner, J.; Kohler, J. M. *Nano Lett.* **2005**, 5, 685

5. V. J. Anderson and H. N. W. Lekkerkerker, *Nature* **2002**, 416, 811.

6. Puntes, V. F.; Krishnan, K. M.; Alivisatos, A. P. *Science* **2001**, *291*, 2115−2117.

7. Yadong, Y. A.; Alivisatos, A. P. *Nature* **2005**, *437*, 664.

8. Kirchner, H. O. K. *Metall. Trans*. **1971**, 2, 2861.

9. Speight, M. V. *Acta Metall.* **1968**, 16, 133.

10. Wagner, C. Z. *Elektrochem.* **1961**, 65, 581.

11. Huang, F.; Zhang, H.; Banfield, J. F. *Nano Lett.* **2003**, 3, 373.

12. P. Fumagalli, C. Spaeth, U. Rudiger, R. J. Gambino, *Ieee Transactions on Magnetics* **1995**, *31*, 3319; R. J. Gambino, P. Fumagalli, *Ieee Transactions on Magnetics* **1994**, *30*, 4461; J. Schoenes, P. Wachter, *IEEE Transactions on Magnetics* **1976**, *12*, 81; P. Wachter, *Handbook on the Physics and Chemistry of Rare Earths, Vol. 2*, North-Holland, Amsterdam, **1979**; N. S. Gaikwad, V. M. Nikale, C. H. Bhosale, *Journal of Physics and Chemistry of Solids* **2003**, *64*, 723; A. B. Henriques, G. D. Galgano, B. L. Diaz, P. H. O. Rappl, E. Abramof, *J. Phys. Condens. Matter* **2007**, *19*, 406234; A. B. Henriques, L. K. Hanamoto, E. Ter Haar, E. Abramof, A. Y. Ueta, P. H. O. Rappl, *International Journal of Modern Physics B* **2004**, *18*, 3813.

13. M. L. Redigolo, D. S. Koktysh, K. van Benthem, S. J. Rosenthal, J. H. Dickerson, *Mater. Chem. and Phys.* **2009**, *115*, 526; M. D. Regulacio, N. Tomson, S. L. Stoll, *Chemistry of Materials* **2005**, *17*, 3114; F. Zhao, H. L. Sun, G. Su, S. Gao, *Small* **2006**, *2*, 244.

14. M. J. Bierman, K. M. Van Heuvelen, D. Schmeisser, T. C. Brunold and S. Jin, *Adv Mater* **2007**, 19, 2677.

15. D. S. Koktysh, S. Somarajan, W. He, M. A. Harrison, S. A. McGill and J. H. Dickerson, Nanotechnology 2010, **21**, 415601.

16. Castro, S. L.; Bailey, S.G.; Banger, K. K.; Hepp, A. F. *J. Phys. Chem. B* **2004,** 108, 12429.

17. Goulet, P. J. G.; Lennox, R. B. *J Am Chem Soc* **2010**, *132*, 9582-9584.

18. Huang, J. X.; Kim, F.; Tao, A. R.; Connor, S.; Yang, P. D. *Nat Mater* **2005**, *4*, 896-900.

19. Laurent, S.; Forge, D.; Port, M.; Roch, A.; Robic, C.; Elst, L. V.; Muller, R. N. *Chem Rev* **2008**, *108*, 2064-2110.

20. Sau, T. K.; Murphy, C. J. *J Am Chem Soc* **2004**, *126*, 8648-8649.

21. Song, H.; Kim, F.; Connor, S.; Somorjai, G. A.; Yang, P. D. *J Phys Chem B* **2005**, *109*, 188-193.

22. Cutler, M.; Mallon, C. E. *J Appl Phys* **1965**, *36*, 201.

23. Tucci, F. C.; Chieffi, A.; Comasseto, J. V.; Marino, J. P. *J Org Chem* **1996**, *61*, 4975-4989.

24. Wang, Z. H.; Wang, L. L.; Huang, J. R.; Wang, H.; Pan, L.; Wei, X. W. *J Mater Chem* **2010**, *20*, 2457-2463.

25. Pola, J.; Urbanova, M.; Volnina, E. A.; Bakardjieva, S.; Subrt, J.; Bastl, Z. *J Mater Chem* **2003**, *13*, 394-398.

26. Nolting, W, *Journal of Physics C-Solid State Physics* **1982**, 15**,** 733-45.

27. Chen W, Zhang X and Huang Y, *Applied Physics Letters,* **2000**, 76, 2328.

28. Kataoka T, Tsukahara Y, Hasegawa Y and Wada Y, *Chemical Communications,* **2005,** 40, 6038.

29. Mirkovic T, Hines M A, Nair P S and Scholes G D, *Chemistry of Materials* 2005, 17, 3451.

30. Y. Hasegawa, T. A. Adachi, A. Tanaka, M. Afzaal, P. O'Brien, T. Doi, Y. Hinatsu, K. Fujita, K. Tanaka, T. Kawai, *Journal of the American Chemical Society* **2008**, 130, 5710.

31. W. He, S. Somarajan, D. S. Koktysh and J. H. Dickerson, *Nanoscale* **2011**, 3, 184-187.

32. Mo, M. S.; Zeng, J. H.; Liu, X. M.; Yu, W. C.; Zhang, S. Y.; Qian, Y. T. *Adv Mater* **2002**, *14*, 1658-1662.

33. Song, J. M.; Lin, Y. Z.; Zhan, Y. J.; Tian, Y. C.; Liu, G.; Yu, S. H. *Cryst Growth Des* **2008**, *8*, 1902-1908.

34. Zhu, Y. J.; Wang, W. W.; Qi, R. J.; Hu, X. L. *Angew Chem Int Edit* **2004**, *43*, 1410-1414.

35. Mahajan S V and Dickerson J H, *Nanotechnology* **2007**, 18, 325605.

36. P. Starynowicz, *Journal of Alloys and Compounds* **2001**, 323, 159.

37. Y. Xu, N. Al-Salim, C. W. Bumby, R. D. Tilley, *Journal of the American Chemical Society* **2009**, 131, 15990.

38. Yan, H.; Cingarapu, S.; Klabunde, K. J.; Chakrabarti, A.; Sorensen, C. M. *Phys Rev Lett* **2009**, *102*, 095501.

39. Shukla, D.; Joshi, A. A.; Mehra, A. *Langmuir* **2009**, *25*, 3786-3793.

40. Hasan, S. A.; Kavich, D. W.; Dickerson, J. H. *Chem Commun* **2009**, 3723-3725.

41. Maenosono, S.; Okubo, T.; Yamaguchi, Y. *Journal of Nanoparticle Research* **2003**, *5*, 5-15.
42. Islam, M. A.; Herman, I. P. *Appl. Phys. Lett.* **2002**, *80*, 3823-3825.

43. Ni, X. M.; Zhao, Q. B.; Zhang, D. G.; Yang, D. D.; Zheng, H. G. *J Cryst Growth* **2005**, *280*, 217-22.

44. Chandrasekharan, N.; Kamat, P. V. *Nano Lett* **2001**, 1, 67-70.

45. W. He and J. H. Dickerson, *Appl. Phys. Lett.* **2011**, 98, 081914.

46. K. S. Cho, D. V. Talapin, W. Gaschler and C. B. Murray, J Am Chem Soc 2005, **127**, 7140.
47. R. L. Penn and J. F. Banfield, *Science* **1998**, 281, 969.

48. F. Huang, H. Z. Zhang and J. F. Banfield, *J Phys Chem B* **2003**, 107, 10470.

49. C. O'Sullivan, R. D. Gunning, A. Sanyal, C. A. Barrett, H. Geaney, F. R. Laffir, S. Ahmed and K. M. Ryan, *J Am Chem Soc* **2009**, 131, 12250.

50. J. Zhang, Y. H. Wang, J. S. Zheng, F. Huang, D. G. Chen, Y. Z. Lan, G. Q. Ren, Z. Lin and C. Wang, *J Phys Chem B* **2007**, 111, 1449.

51. K. M. Ryan, A. Mastroianni, K. A. Stancil, H. T. Liu and A. P. Alivisatos, *Nano Lett* **2006**, 6, 1479.

52. W. F. Brown, Jr., *J. Appl. Phys.* **1968,** 39, 993.

53. R. P. Cowburn, D. K. Koltsov, A. O. Adeyeye, M. E. Welland, D. M. Tricker, *Phys. Rev. Lett.* **1999**, 83, 1042.

54. J. I. Gittleman, B. Abeles, and S. Bozowski, *Phys. Rev. B* **1974**, 9, 3891.

55. C. P. Bean and J. D. Livingston, *J. Appl. Phys.* **1959**, **30**, 120.

56. S. I. Woods, J. R. Kirtley, S. Sun, and R. H. Koch, *Phys. Rev. Lett.* **2001**, 87, 137205.

57. S. H. Huh, A. Nakajima, and K. Kaya, *J. Appl. Phys.* **2004**, 95, 2732.

58. S. Mørup and E. Tronc, *Phys. Rev. Lett.* **1994**, 72, 3278.

59. C. Gilles, P. Bonville, H. Rakoto, J. M. Broto, K. K. W. Wong, S. Mann, *Journal of Magnetism and Magnetic Materials* **2002**, *241*, 430.

60. Shafi, K. V. P. M.; Ulman, A.; Yan, X.; Yang, N.-L.; Estournes, C.; White, H.; Rafailovich, M.*Langmuir* **2001**, *17*, 5093.

61. D. Resnick, K. Gilmore, Y. U. Idzerda, M. Klem, E. Smith, and T. Douglas, *J. Appl. Phys.* **2004**, 95, 7127.

62. Andrew T. Heitsch, Doh C. Lee† and Brian A. Korgel, *J. Phys. Chem. C* **2010**, *114*, 2512.
63. H. Reiss, *J. Chem. Phys.* **1951**, *19*, 482.

64. J. X. Gao, C. M. Bender, C. J. Murphy, *Langmuir* **2003**, *19*, 9065; L. Manna, L. W. Wang, R. Cingolani, A. P. Alivisatos, *Journal of Physical Chemistry B* **2005**, *109*, 6183.

65. C. Gilles, P. Bonville, H. Rakoto, J. M. Broto, K. K. W. Wong, S. Mann, *Journal of Magnetism and Magnetic Materials* **2002**, *241*, 430; A. T. Heitsch, D. C. Lee, B. A. Korgel, *The Journal of Physical Chemistry C* **2010**, *114*, 2512.